SUPPORTING INFORMATION

Electrochemically Synthesized Amorphous and Crystalline Nanowires: Dissimilar Nano-mechanical Behavior in Comparison to Homologous Flat Films

Muhammad A. Zeeshan, Daniel Esqué–de los Ojos, Pablo Castro-Hartmann, Miguel Guerrero, Josep Nogués, Santiago Suriñach, Maria D. Baró, Bradley J. Nelson, Salvador Pané, Eva Pellicer, Jordi Sort

Additional details on Experimental Methods

Preparation of AAO templates

The AAO templates were obtained by one-step anodic oxidation of ~2 μm aluminium e-beam evaporated onto a 0.5 cm^2 Si (111) / Ti (6 nm) /Au (12 nm) substrate. The Si backside was protected with a 1 μm-thick SiO_2 insulating layer by means of plasma-enhanced chemical vapour deposition. The anodization was performed in a one-compartment two-electrode cell in 0.3 M oxalic acid at a constant potential of +60 V. A lead sheet was used as the cathode. Distilled water from a cryostat was circulated in the outer jacket of the cell to maintain the working temperature at 5 °C. In order to minimize both concentration and thermal gradients, continuous bubbling of N_2 through the electrolyte was used. After anodization, the samples were rinsed with Millipore Milli-Q water and subsequently kept in a 5 wt% H_3PO_4 solution for 45 min at room temperature to allow for pore widening and barrier layer thinning. A scheme of the synthesis procedure,

involving the anodization of the Al film and the subsequent deposition of the CoNi(Re)P nanowires, is shown in Figure 1.

Electrodeposition of CoNiReP and CoNiP nanowires and films

The CoNi(Re)P NWs were grown inside the pores of home-made anodized aluminium oxide (AAO) templates. To promote uniform filling of the pores, the pulse current (PC) electrodeposition mode was used. After electrodeposition, the AAO templates were dissolved in NaOH and the released NWs were observed both by field-emission scanning electron microscopy (FESEM) and transmission electron microscopy (TEM). Quantitative compositional analyses were performed by energy-dispersive X-ray (EDX) spectroscopy. Representative results are shown in Fig. S1. Continuous films of CoNi(Re)P (3 μm in thickness) with an analogous composition and microstructure as the NWs were obtained in the same electrolytes (Table S1) by reverse pulse current (RPC) on Si (111) / Ti (100 nm) /Au (125 nm) 5 mm x 6 mm substrates. Before electrodeposition the gold surface was degreased by first dipping it in acetone, followed by isopropanol, and, finally, water. The cathodic pulse current densities, j_c, ranged between –15 and –100 mA^{-2} cm with a pulse duration of t_c = 1 ms; the anodic pulse current density, j_a, was $j_a = |-j_c|/2$, with a pulse duration of t_a = 1 ms (duty cycle, $\gamma' = 0.5$). The charge density was kept at –8.8 C cm^{-2} for all depositions. Deposition was conducted under gentle stirring (500 rpm) to ensure homogeneous composition throughout the film thickness. Higher current densities were needed to attain a similar composition in NWs as compared to continuous films. This was anticipated for three reasons: (i) the electric conductivity inside the AAO pores is significantly lower than in the flat conductive seed layer used for the electrodeposition of films, (ii) diffusion of all ionic species present in the electrolytic bath inside the pores is challenging, (iii) hydrogen bubbles created during the growth of the alloys need to escape from inside the pores, thus slowing the electrodeposition process.

Composition, morphological and structural characterization

The length of the NWs was determined using a Zeiss NVision 40 field emission scanning electron microscope (FESEM) equipped with a focused ion beam (FIB). The chemical composition of the samples was analyzed by energy dispersive X-ray spectroscopy (EDX) on a Zeiss Merlin FESEM at 15 kV along the NW length to ensure compositional homogeneity. Representative results are shown in Fig. S1. X-ray diffraction (XRD) patterns were obtained with a Philips X'Pert diffractometer using the Cu K_α radiation in the 30º-90º 2θ range (0.03º step size, 8 s holding time). Transmission electron microscopy (TEM) observations of the NWs were carried out on a Jeol JEM-2011 at 200 kV. The AAO templates were dissolved in 2 M NaOH, and the released NWs were then rinsed with 95% ethanol in order to avoid reprecipitation of alumina. One or two drops of freshly-prepared suspension were placed drop-wise onto carbon coated Cu TEM grids. The XRD patterns of the samples are shown in Figure S2. In all cases peaks from the Ti and Au seed-layers and the substrate (Si/Ti/Au) are observed, along with a small peak from the sample holder (steel) and the response from the NWs themselves. No peaks from AAO are observed since the templates are amorphous.

Sample preparation prior to nanoindentation studies

The extremely small lateral dimensions of nano-sized objects make their mechanical characterization challenging. Nanotensile tests are costly and complex to implement, since they generally require in-situ electron microscopy observations. Nanoindentation is a suitable characterization method, but technical hurdles arise when fixing nanoscale samples to the substrate. Specifically, welding a nanowire from its edges can induce residual stress concentrations along its length, which, in turn, creates artifacts in the measurements. To avoid rolling of the NWs during indentation, the NWs were fixed onto the surface of TEM grids with a

gluing procedure. The reference finder grids (London Finder) and adhesive pen for grids were purchased from Ted Pella. A support film was made by covering the TEM grids with a relatively-thick evaporated carbon layer (using a Baltec MED 020 evaporator). Subsequently, the adhesive was used to provide a flat, thin, rigid layer of adherent coating on the carbon grids. Finally, a drop of suspension with properly dispersed NWs was placed drop-wise onto the surface of the adherent coating, and the samples were left to dry in air for at least 24h prior to nanoindentation. The adherent coating provided good rigidity to the TEM grid preventing from deflection during the nanoindentation experiments. TEM was used to visualize the NWs and select pre-defined locations for the indentation to be subsequently performed. The Cu grid containing the nanowires was placed under an atomic force microscopy mounted on the same table as the indenter. After confirming the location of a target nanowire, an array of 2 x 2 indentations separated by 0.5 μm, was created around the position of the nanowire, and subsequent atomic force microscopy imaging was used to verify that the nanowire had actually been indented. The mechanical properties were extracted from the test corresponding to the nanoindentation of the nanowire. Sometimes the nanoindentation was not successful (*i.e.*, not performed exactly at the central part of the nanowire but on an edge). Such curves were disregarded from the analysis.

Additional details on analysis methods

Effect of the curvature of the nanowires on the contact area, hardness and Young's modulus

Most previous studies reporting on the values of indentation hardness and Young's modulus of nanowires use the conventional method of Oliver and Pharr to extract these parameters, considering the nanowires as flat surfaces. Only a few authors have taken into account the curvature of the nanowires when estimating the contact area. To a first approximation, one can use simple geometrical reasoning, including the actual tip radius (250 nm) and the diameter of

the nanowires (100 nm), to estimate how the contact area (and therefore the hardness) is modified compared to an indentation on a flat surface. Figure S3 depicts the geometry of the system, considering that the nanowire is completely rigid (*i.e.*, no barrelling effects are taken into account in this simple picture). The figure shows that the contact area at maximum depth estimated using the method of Oliver and Pharr (πa^2) is much larger than the real contact area on the curved surface of the nanowire ($\pi a'^2$). The distance a' can be calculated from the radius of the nanowire (R_{NW}) and the maximum depth (h_{max}):

$$(a')^2 + (R_{NW}-h_{max})^2 = R_{NW}^2 \qquad \text{(Equation S1)}$$

Using the experimental value of maximum penetration depth (corresponding to the maximum applied load, P_{max} = 0.18 mN) for the amorphous nanowires ($h_{max} \approx 20$ nm) the value of contact radius is a' ≈ 40 nm. Thus, the contact area at maximum depth is approximately 5026 nm^2 in this particular sample, which would result in a mean contact pressure of approximately 36 GPa, hence, much larger than the hardness evaluated using the method of Oliver and Pharr, *i.e.*, considering the nanowire as a flat surface, H = 7.6 GPa. Similarly, based on the ratio a/a' and the resulting correction for the contact area, the Young's modulus of the nanowires would be a factor 2.4 larger than the value estimated using the model of Oliver and Pharr. Analogous corrections would hold for crystalline nanowires. Nevertheless, these values are considerably overestimated (as is evidenced by 3D FEM), because they do not take into account sink-in effects or the barrelling of the nanowires. These effects, together with specific properties of the different types of nanowires (amorphous vs. crystalline) and the effects of lack of lateral confinement, are all considered in the finite element simulations.

Additional details on the finite element simulations

Three-dimensional (3D) FEM was performed using the ABAQUS software, taking into account the actual geometry of the nanowires, as depicted in Figure S4. The Mohr-Coulomb yield criterion was used for the amorphous film and nanowires, whereas the crystalline materials were modelled using the Tresca criterion. Since the geometry of the nanowire is not symmetric in the 3D space, it is important to use 3D finite element simulations. The actual rounding of the tip (R_{tip} = 250 nm) has been incorporated in the simulations. Both a rigid substrate and an elastic substrate (with Young's modulus of 200 GPa) were considered in the simulations of the nanowires. Different values of the friction coefficient between the tip and the sample (μ = 0, 0.1 and 0.3) were attempted, but this parameter had virtually no influence on the resulting load-displacement indentation curves. Hence, all results included in the manuscript correspond to μ = 0. The mesh used for the FEM of the film indentation consisted of 9362 fully-integrated brick-shaped elements, whereas for the NWs the model comprised 36542 fully-integrated brick-shaped elements. In both cases the rounded Berkovich tip was modelled as a rigid rounded conical indenter with an apical angle of 70.3º. For the NWs simulations, a "tied" constraint was defined between the substrate and the line of nodes of the NW in contact with it.

Effect of lateral confinement and correlation between hardness, yield stress and cohesive stress

The effect of lateral confinement during nanoindentation, *i.e.*, mechanical confinement exerted by the surrounding matrix on the localized indented regions, is important when comparing the results from nanoindentation with those of macroscopic compression tests. This effect is present in the continuous thick films, but it is essentially absent in the nanowires since they are not embedded in a matrix. During nanoindentation of bulk material, yielding is primarily governed by the shear component of the applied stress. The mean contact pressure in an indentation test is higher than the one required to initiate plastic flow in a uniaxial compression experiment (that is,

the compressive yield stress, σ_y), because there is an influence of the hydrostatic pressure from the surrounding matrix. As a result there exists a so-called "constraint factor" (C) between the hardness (mean contact pressure during indentation) and the uniaxial compressive yield stress so that $H = C\sigma_y$. Typically, C is between 2.7 and 3 for metallic alloys. In the nanowires, since the compressive effect from the surrounding matrix does not exist, it can be assumed that $C \approx 1$, *i.e.*, the indentation hardness is similar to the uniaxial compressive yield stress.

In materials whose yielding is governed by the Mohr-Coulomb criterion, the yield stress can be estimated from the values of cohesive stress and friction coefficient (see for example Ref. 26):

$$\sigma_y = \frac{2ccos(arctan\beta_{M-C})}{1 - \sin(arctan\beta_{M-C})} \qquad \text{(Equation S2)}$$

For the amorphous continuous film, taking c = 2 GPa and $\beta_{M\text{-}C} = 0.194$, a yield stress $\sigma_y = 4.8$ GPa is obtained. Since the constraint factor in metallic alloys is typically between 2.7 and 3, the hardness value ($H = C\sigma_y$) for the films is between 13 and 14.4 GPa, which is not far from the hardness directly estimated using the contact area determined from the 3D finite element simulations (H_{Sim} = 12 GPa). In the case of the amorphous nanowires, Equation S2 with c = 9 GPa, and $\beta_{M\text{-}C} = 0.123$ gives $\sigma_y = 20.3$ GPa. This value is also close to the hardness directly estimated from the simulations, *i.e.*, from the simulated contact area, which is H_{Sim} = 23 GPa (Table 1). This confirms that the constraint factor in small sized metallic glasses, $C = H/\sigma_y$, is close to 1.

Strain rate effects

No pop-in events are visible in the loading segments of the nanoindentation curves corresponding to the amorphous alloys. The loading rate for the measurements was approximately 1 x 10^{-2} mN/s for all samples. The indentation strain rate achieved at the end of

the loading segment, $\dot{\varepsilon}$, varied between 2 x 10^{-2} and 5 x 10^{-2} s^{-1}, depending on the sample. Hence, the corresponding effective shear strain rate, $\dot{\gamma}_{eff} = 0.16\,\dot{\varepsilon}$, varied between 3 x 10^{-3} and 8 x 10^{-3} s^{-1}. Thus, according to the deformation map proposed by Schuh et al. (Ref. 31), the investigated metallic glass should undergo inhomogeneous plastic flow at room temperature for this range of indentation strain rates. However, the amorphous film and NWs undergo homogeneous deformation for these indentation conditions, suggesting that the small indentation plastic zone resulting from the low maximum load used for nanoindentation avoids the full development of shear bands in both systems.

Additional results on crystalline CoNi(Re)P alloys

Results from 3D finite element simulations performed on the crystalline nanowires and film

3D finite element simulations have been used to estimate the hardness of the crystalline films and nanowires (using the Tresca yield criterion). However, in this case the agreement between the experimental and simulated curves is not strong, particularly for the nanowires where the penetration depth was typically overestimated, even when assuming a high yield stress, which caused the load/unload curves to fully overlap (see Figures S5 and S6). The use of the Mohr-Coulomb yield criterion did not improve the discrepancy between experimental and calculated indentation curves. The difficulty of properly adjusting the nanoindentation curves of the crystalline materials stems from the very low penetration depths, typically only 2-3 times the crystallite size, so that sophisticated crystal plasticity models, taking into account the generation and pile-up of dislocations as well as strain gradient effects, may be needed to account for the observed plastic flow. Such modelling is beyond the scope of this manuscript, which places its main emphasis on understanding the properties of the amorphous film/nanowires. In any case, it is clear that the relative increase of hardness between the nanocrystalline films and nanowires is much larger than that observed between the amorphous films and nanowires, as indicated in

Table 1, where the approximate values of the mean contact pressure at the end of the loading segment have been included.

Comparison of mechanical properties between the crystalline nanowires and the corresponding films

Studies on Co single-crystals showed that H and E_r are larger when measured on the (002) planes than on any other crystallographic plane (Refs. 32,33). However, if the (200)-textured $Co_{75}Ni_{11}Re_8P_6$ alloy is considered, one would expect lower H in the NWs, since H is measured in that case perpendicular to the preferred (002) direction. Furthermore, the average crystallite sizes of the quaternary film and NWs are not significantly different (Supporting Figure S2). There is an unusually large variation in the strength of the Re-free NWs with respect to the value in the corresponding flat continuous films. Careful inspection of the XRD and electron diffraction patterns reveals that such "anomalous" variation could be due to the fact that the microstructure of the Re-free NWs and film is not strictly identical. While relatively well-defined XRD peaks are observed in the Re-free film [see, for example, the (101) peak located at ~47.5º], the XRD peaks corresponding to the Re-free NWs are more diffuse and broader, suggesting that the microstructure is more refined (*i.e.*, smaller crystallite size) in the NWs. Evidence for the ultra-nano-crystalline character of the Re-free NWs is also obtained from electron diffraction patterns (see Fig. 3e). Hence, the origin of the large increase of H in the Re-free NWs could be two-fold: (i) a sample size effect and (ii) a refinement of grain size and subsequent pile-up of dislocations at grain boundaries.

The increase of H in nano-sized crystalline objects with respect to the bulk behaviour has been reported in recent years by various authors (Refs 3-6). The effect is mainly ascribed to the decrease in the amount of structural defects within the nano-objects and the hindrances imposed by the finite material volume on dislocation motion. Our results also reveal that H for the

crystalline $Co_{79}Ni_{11}P_{10}$ NWs is significantly lower than that of the $Co_{44}Ni_{30}Re_{12}P_{14}$ NWs. This highlights the importance of Re incorporation (one of the most mechanically hard metals found in nature) on the nanomechanical behaviour of the investigated alloys. Contrary to H, E does not critically depend on the sample size, since elastic deformation is mainly determined by chemical bonding. This is in agreement with the observations made on SiC nanorods (Ref. 34) or Ag NWs (Ref. 21), although some authors have also reported a considerable decrease of E in nano-sized ceramic materials (*e.g.*, $Al_4B_2O_9$ [Ref. 22] or ZnS [Ref. 35]), where nano-cracks easily appear during plastic deformation. Concerning the plasticity index, the decrease observed in the NWs could be the result of reduced dislocation activity in samples with reduced dimensions, where plastic flow could start to be influenced by partial dislocations nucleated from surface steps, as recently reported for 10-nm size nanocrystals (Ref. 36).

Table S1. Electrolyte composition used for the deposition of CoNiReP and CoNiP NWs and films.

		CoNiReP	**CoNiP**
Species	**Chemical**	**concentration (mol dm^{-3})**	**concentration (mol dm^{-3})**
Metal salts	$CoSO_4 \cdot 7H_2O$	0.05	0.05
	$NiSO_4 \cdot 6H_2O$	0.03	0.03
	$NiCl_2 \cdot 6H_2O$	0.02	0.02
	$NaH_2PO_2 \cdot H_2O$	0.02	0.02
	NH_4ReO_4	0.01	0
Complexing agents	NH_2CH_2COOH (glycine)	0.05	0.05
	$C_6H_5Na_3O_7 \cdot 2H_2O$ (sodium citrate)	0.05	0.05
Electrolyte support	Na_2SO_4	0.5	0.51
Additives	$Ce_2(SO_4)_3$	$2 \cdot 10^{-5}$	$2 \cdot 10^{-5}$
	Tergitol 08	2.5 (ml dm^{-3})	2.5 (ml dm^{-3})
	L-ascorbic acid	$8.5 \cdot 10^{-3}$	$8.5 \cdot 10^{-3}$
	$C_7H_4NNaO_3S \cdot 2H_2O$ (sodium saccharinate)	0.005	0.005

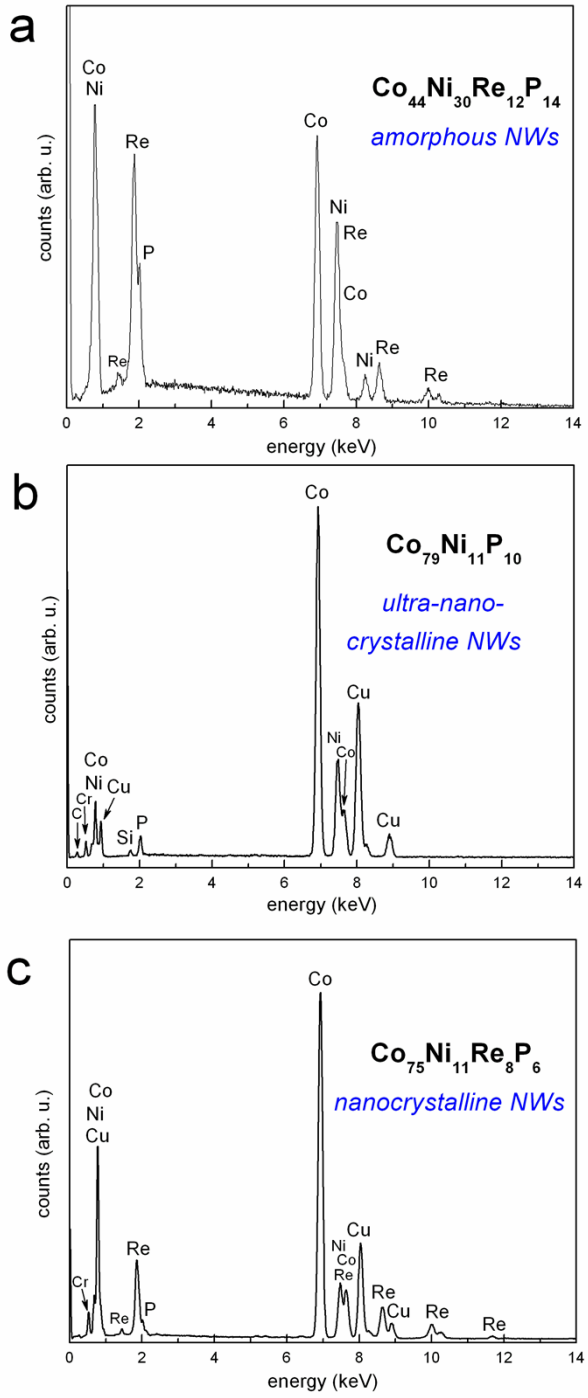

Figure S1. Energy-dispersive X-ray analyses corresponding to the compositional analyses of the electrodeposited NWs selected for nanomechanical studies: **(a)** $Co_{44}Ni_{30}Re_{12}P_{14}$, **(b)** $Co_{79}Ni_{11}P_{10}$, **(c)** $Co_{75}Ni_{11}Re_8P_6$.

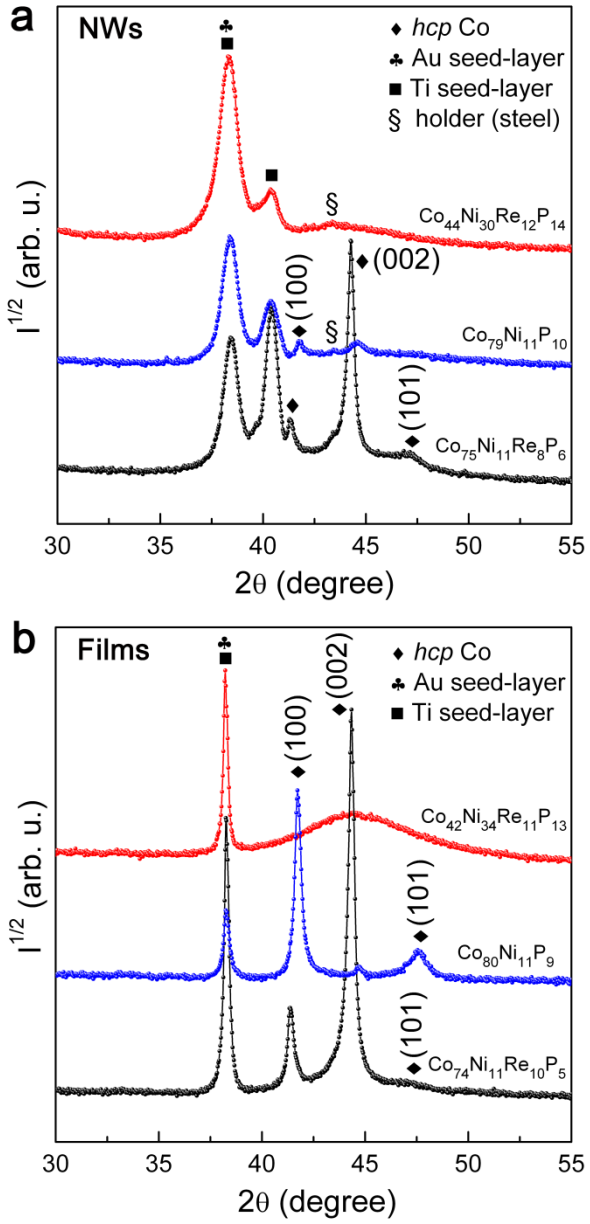

Figure S2. X-ray diffraction (XRD) patterns corresponding to: **(a)** arrays of NWs electrodeposited inside the AAO templates and **(b)** continuous electroplated films with analogous compositions as the NWs. Note that the Miller indices of the XRD peaks of the crystalline alloys (which are hexagonal close compact, hcp) are designated. Also indicated are the reflexions from the adhesion (Ti) and seed (Au) layers, as well as tiny peaks coming from the XRD holder.

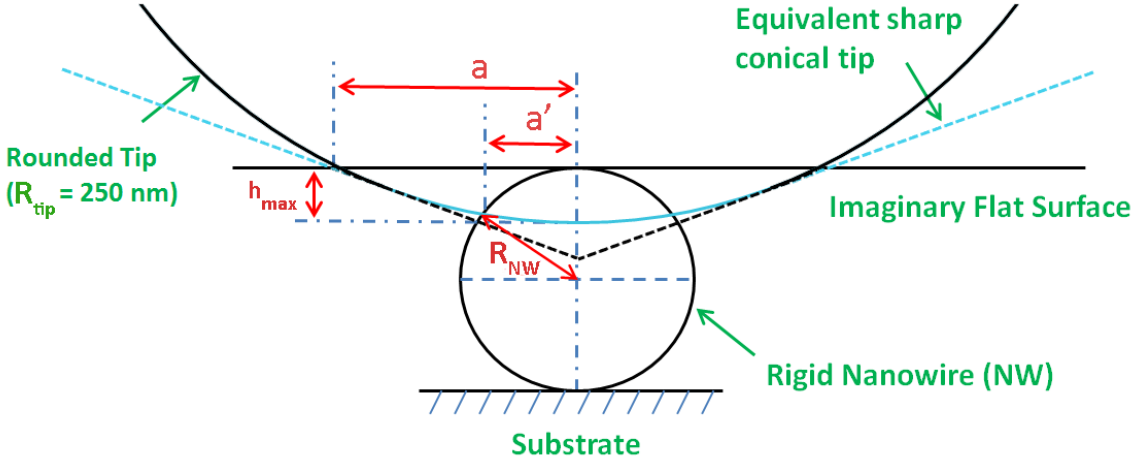

Figure S3: Schematic drawing of the contact between the indenter and the nanowire. The "ideal" Berkovich indenter is depicted here as an equivalent conical tip with an effective cone angle of 70.3º [see: A.C. Fischer-Cripps, Nanoindentation, Second Edition, Springer, New York, 2004 (page 6)]. The "real" (*i.e.*, blunted) indenter tip is more similar to a spherical tip with a radius of 250 nm. The dimensions of the nanowire and the tip are drawn to scale. The contour of the cono-spherical indenter that best approaches the real tip used in our study is drawn in cyan.

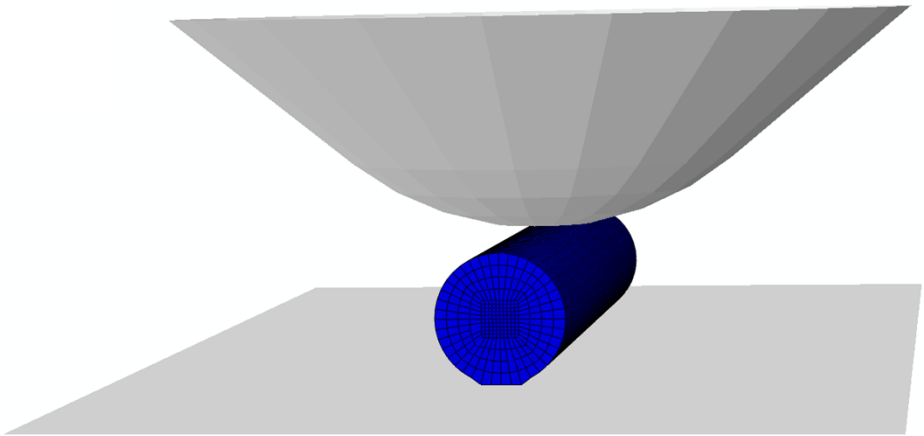

Figure S4: Schematic drawing of the geometry used for the finite element simulations of the nanoindentation of the nanowires. The nanowire and the indenter tip (with the corresponding rounding) are drawn to scale.

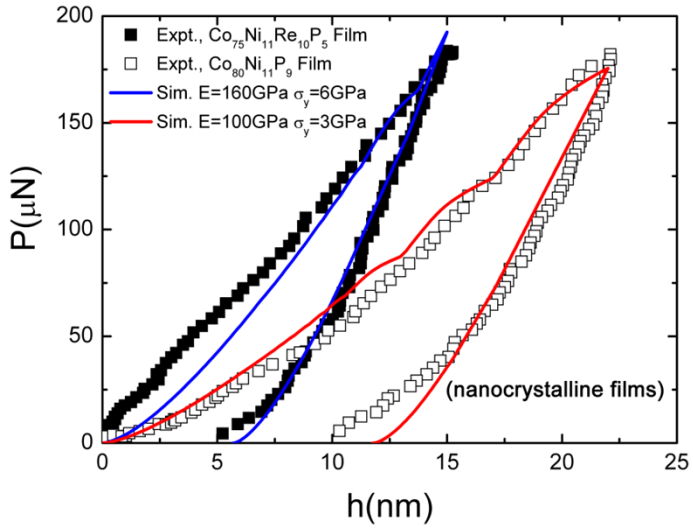

Figure S5: Representative load-displacement experimental nanoindentation curves corresponding to the $Co_{75}Ni_{11}Re_{10}P_5$ and $Co_{80}Ni_{11}P_9$ *crystalline films*, together with the 3D finite element simulations obtained using the Tresca yield criterion with yield stress and Young's modulus indicated in the figure.

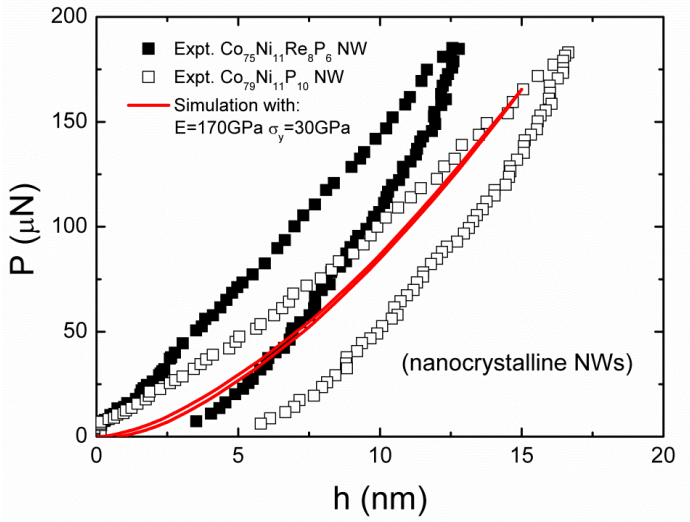

Figure S6: Representative load-displacement experimental nanoindentation curve corresponding to the $Co_{75}Ni_{11}Re_8P_6$ and $Co_{79}Ni_{11}P_{10}$ *nanocrystalline nanowires*, together with a 3D finite element simulation obtained using the Tresca yield criterion with a yield stress of 30 GPa and a Young's modulus of 170 GPa.

Movie V1: Evolution of the Tresca stress contour mapping during nanoindentation of the amorphous $Co_{42}Ni_{34}Re_{11}P_{13}$ 3 μm-thick film, as determined from 3D finite element simulations. The scale bar is in Pa.

Movie V2: Evolution of the Tresca stress contour mapping during nanoindentation of an amorphous $Co_{44}Ni_{30}Re_{12}P_{14}$ nanowire, as determined from 3D finite element simulations. The scale bar is in Pa.